Chemical Science

ROYAL SOCIETY OF CHEMISTRY

EDGE ARTICLE

View Article Online
View Journal | View Issue

Cite this: *Chem. Sci.*, 2024, **15**, 6410

All publication charges for this article have been paid for by the Royal Society of Chemistry

Ultrafast photophysics of an orange–red thermally activated delayed fluorescence emitter: the role of external structural restraint†

Yixuan Gao,[a] Yaxin Wang,[a] Zilong Guo,*[a] Yan Wan,[c] Zheng Xue,[b] Yandong Han,[b] Wensheng Yang[ab] and Xiaonan Ma*[a]

Received 19th January 2024
Accepted 21st March 2024

DOI: 10.1039/d4sc00460d

rsc.li/chemical-science

The application of thermally activated delay fluorescence (TADF) emitters in the orange–red regime usually suffers from the fast non-radiative decay of emissive singlet states (k_{NR}^{S}), leading to low emitting efficiency in corresponding organic light-emitting diode (OLED) devices. Although k_{NR}^{S} has been quantitatively described by energy gap law, how ultrafast molecular motions are associated with the k_{NR}^{S} of TADF emitters remains largely unknown, which limits the development of new strategies for improving the emitting efficiency of corresponding OLED devices. In this work, we employed two commercial TADF emitters (**TDBA-Ac** and **PzTDBA**) as a model system and attempted to clarify the relationship between ultrafast excited-state structural relaxation (ES-SR) and k_{NR}^{S}. Spectroscopic and theoretical investigations indicated that S_1/S_0 ES-SR is directly associated with promoting vibrational modes, which are considerably involved in electronic–vibrational coupling through the Huang–Rhys factor, while k_{NR}^{S} is largely affected by the reorganization energy of the promoting modes. By restraining S_1/S_0 ES-SR in doping films, the k_{NR}^{S} of TADF emitters can be greatly reduced, resulting in high emitting efficiency. Therefore, by establishing the connection among S_1/S_0 ES-SR, promoting modes and k_{NR}^{S} of TADF emitters, our work clarified the key role of external structural restraint for achieving high emitting efficiency in TADF-based OLED devices.

Introduction

Organic light-emitting diode (OLED) technology is becoming increasingly attractive due to its great potential for ultra-high definition (UHD) displays.[1–5] As a key factor in the performance of OLED devices, external quantum efficiency (η_{EQE}) is described as the ratio between the number of emitted photons and number of injected carriers. In most cases, the η_{EQE} of OLED devices can be expressed as the product of several contributing terms:[6,7]

$$\eta_{EQE} = \gamma \times \eta_{EUE} \times \Phi_F \times \eta_{out} \quad (1)$$

where the carrier balance factor (γ) and output coupling factor (η_{out}) are associated with the device design and fabrication, respectively, while exciton utilization efficiency (η_{EUE}) and fluorescent quantum yield (Φ_F) are regarded as intrinsic properties of the emitters and are associated with corresponding excited-state processes. Spin statistics show that the recombination of injected electrons and holes leads to 25% singlet and 75% triplet states in OLED emitting layers, respectively,[8,9] while η_{EUE} gives the fraction of excited states that can decay to the ground state radiatively. Since $T_1 \rightarrow S_0$ decay is spin-forbidden, η_{EUE} is largely determined by the quantum yield (Φ_{RISC}) of the reverse intersystem crossing (RISC, $T_1 \rightarrow S_0$, with rate constant of k_{RISC}), which competes with other T_1 relaxation routes (radiative k_R^T and non-radiative k_{NR}^T, Fig. S1†):[10,11]

$$\eta_{EUE} \propto \Phi_{RISC} = \frac{k_{RISC}}{k_{RISC} + k_R^T + k_{NR}^T} \quad (2)$$

Enormous efforts have been made towards designing thermally activated delayed fluorescence (TADF) emitters with minimized singlet–triplet energy gap (ΔE_{ST}) and enhanced spin–orbit coupling (SOC) to enable thermal conversion of $T_1 \rightarrow S_1$, which can potentially push η_{EUE} to ~100%.[12–15] Since the k_{RISC} of TADF emitters is usually on a time scale of 10^3–10^5 s^{-1}, η_{EUE} is generally associated with slow dynamics of TADF emitters, which has been intensively investigated.[14,16–18]

In addition to the efficient utilization of current-generated triplet states, the Φ_F of TADF emitters greatly affects the η_{EQE} of the corresponding OLED devices, which describes the ratio of singlet (S_1) states that can be radiatively relaxed to the S_0 state, *i.e.*, competing plausible relaxation channels for the S_1 state (Fig. S1†):[19–21]

[a]*Institute of Molecular Plus, Tianjin University, Tianjin 300072, P. R. China. E-mail: xiaonanma@tju.edu.cn; zilong.guo@tju.edu.cn*

[b]*Engineering Research Center for Nanomaterials, Henan University, Kaifeng 475004, P. R. China*

[c]*College of Chemistry, Beijing Normal University, Beijing 100875, P. R. China*

† Electronic supplementary information (ESI) available. See DOI: https://doi.org/10.1039/d4sc00460d

$$\Phi_F = \frac{k_R^S}{k_R^S + k_{NR}^S + k_{ISC}} \quad (3)$$

In addition, Φ_F includes a contribution from the S_1 state directly generated by injected carriers (Φ_{PF}, prompt fluorescence) and converted from the T_1 state (Φ_{DF}, delayed fluorescence):

$$\Phi_F = \Phi_{PF} + \Phi_{DF} \quad (4)$$

For organic TADF emitters, k_{ISC} is usually slow (10^7–10^8 s^{-1}),[16,22] for which the presence of rapid non-radiative decay is a key factor that can significantly reduce the Φ_F of TADF emitters. In a weak coupling regime, the rate constant of the S_1 state non-radiative decay (k_{NR}^S) with energy gap ($\Delta E_{S_1-S_0}$) and electronic coupling (C) can be described as[23–25]

$$k_{NR}^S = \frac{C^2\sqrt{2\pi}}{\hbar\sqrt{\hbar\omega_M \Delta E_{S_1-S_0}}} \exp\left\{ -\frac{\Delta E_{S_1-S_0}}{\hbar\omega_M}\left[\ln\left(\frac{\Delta E_{S_1-S_0}}{l\lambda_M}\right) - 1\right]\right\} \quad (5)$$

where ω_M and λ_M represent the frequency and reorganization energy contribution of the promoting vibrational mode, while l is the number of involved vibrational modes. By assuming $l = 1$, eqn (5) can be simplified to the famous energy gap law with the molecule-specific parameter γ as[21,25–27]

$$k_{NR}^S \propto \exp\left(-\frac{\gamma \Delta E_{S_1-S_0}}{\hbar\omega_M}\right) \quad (6)$$

which indicates that k_{NR}^S increases exponentially with the reduction of the $S_1 \rightarrow S_0$ energy gap ($\Delta E_{S_1-S_0}$), leading to challenges in the design of long-wavelength TADF emitters with high Φ_F.[28–31] As a result, reported TADF emitters in the blue to green regime largely exhibit considerably high Φ_F,[32–34] while the η_{EQE} of the corresponding OLED devices are primarily affected by RISC. In contrast, the small $\Delta E_{S_1-S_0}$ of orange–red TADF emitters leads to fast k_{NR}^S competing with the radiative decay of the S_1 state, resulting in a low Φ_F and subsequently an unsatisfactory η_{EQE} for OLED devices, although up to 100% η_{EUE} can be expected *via* efficient RISC.[19,28,35–37]

Recently, enormous efforts have been made towards developing long-wavelength TADF-based OLED devices with a high η_{EQE},[28,35] in which the low Φ_F of TADF emitters is usually regarded as the main obstacle.[28,38–40] Therefore, one can expect opportunities to further improve the η_{EQE} of TADF-based long-wavelength OLED devices by somehow effectively slowing down the k_{NR}^S rate.[41–44] Recently, Kwon and co-workers reported an acceptor–donor–acceptor (ADA) type TADF emitter (**PzTDBA**, Scheme 1) and realized >30% of the η_{EQE} of orange–red OLED devices.[45] Although the excited-state mechanism that is responsible for the high η_{EQE} is still ambiguous, the reported ~100% Φ_F of **PzTDBA** in doping films indicates that non-radiative decay of the S_1 state is nearly terminated, which seems to violate the well-known energy gap law (eqn (6)). Therefore, understanding the underlying ultrafast photophysics that is associated with the slow k_{NR}^S of **PzTDBA** might provide inspiration for designing high-performance TADF emitters in the long-wavelength regime.

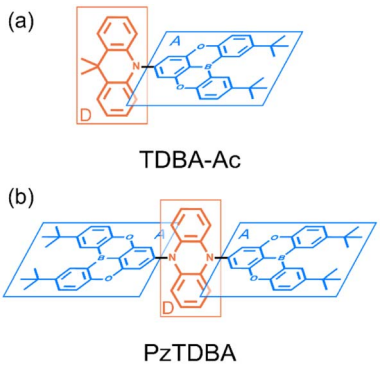

Scheme 1 Illustrated chemical structure of investigated TADF emitters: (a) **TDBA-Ac**, D–A type; (b) **PzTDBA**, A–D–A type. The charge donors and acceptors are displayed in blue and red, respectively.

In this work, the ultrafast photophysics of an orange–red TADF emitter (**PzTDBA**, ADA-type) and its DA-type analogue (**TDBA-Ac**, deep-blue) was investigated using femtosecond transient absorption (fs-TA), time-resolved fluorescence (tr-FL) and theoretical vibrational analysis.[46] Compared with the one-step D–A twisting of the **TDBA-Ac** emitter, **PzTDBA** exhibits two-step S_0/S_1 excited-state structural relaxation (ES-SR), *i.e.* fast D–A twisting and slow planarization of the Pz group. The promoting vibrational modes associated with the S_0/S_1 ES-SR motions of the **TDBA-Ac** and **PzTDBA** emitters were theoretically identified, which dominate the electronic-vibrational coupling (EVC) of the S_1 state. Meanwhile, promoting modes contribute to fast k_{NR}^S through the corresponding reorganization energy contribution (λ_M). In doping films, the S_0/S_1 ES-SR motions of **PzTDBA** are suppressed by external structural restraint, which greatly slows down k_{NR}^S and leads to ~100% Φ_F. Our work established the connection among the S_0/S_1 ES-SR, promoting modes and S_1 state non-radiative decay and indicated the key role of medium rigidity in improving the emitting efficiency of TADF emitters, which should provide inspiration for the future development of TADF emitters.

Results and discussion

Low-lying excited states and steady state spectra

Fundamental photophysics of **TDBA-Ac** and **PzTDBA** emitters were first investigated in solvents with different polarities (Table S1†). In OLED devices, TADF emitters are usually doped in a wide-bandgap organic semiconductor as the host. To avoid multi-photon excitation of the host in fs-TA experiments, we prepared doping films (2 wt%) of TADF emitters by employing polystyrene (PS) as the host, and the polarity of the PS medium ($\varepsilon = 2.6$–2.7, $\Delta f = 0.03$) was determined to be comparable with toluene (Fig. S2†).[47,48] The UV/Vis absorption and fluorescence spectra of the **TDBA-Ac** and **PzTDBA** emitters in various solutions and films (2 wt%) can be seen in Fig. 1 and S3.† The TD-DFT (M06-2X/6-311G**, PCM = toluene) calculated vertical low-lying singlet and triplet states (S_1–S_3, T_1–T_3) are listed in Table S2† with the visualized distribution of frontier orbitals (HOMO−2 to LUMO+2) shown in Table S3.† The lowest-lying S_1

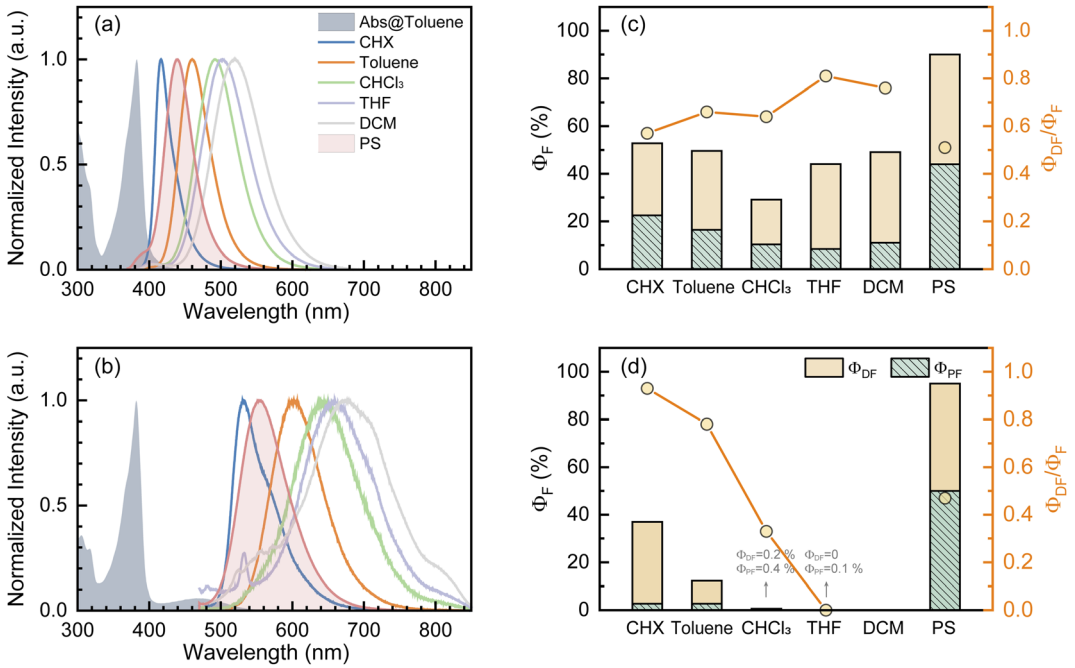

Fig. 1 The steady UV/vis absorption and fluorescence spectra of **TDBA-Ac** (a) and **PzTDBA** (b) in various solutions and PS doping films. Measured total fluorescence quantum yield (Φ_F), corresponding prompt (Φ_{PF}) and delayed (Φ_{DF}) contribution, as well as the related contribution of the delayed component (Φ_{DF}/Φ_F) of **TDBA-Ac** (c) and **PzTDBA** (d).

states of **TDBA-Ac** and **PzTDBA** are dominated by the H → L transition, corresponding to the charge transfer state (noted as $^1CT_{DA}$) with low oscillator strength, which can be seen as weak absorption of **TDBA-Ac** (400–450 nm) and **PzTDBA** (420–540 nm). Upon UV excitation, solvatochromism was observed for **TDBA-Ac** and **PzTDBA**, indicating that the fluorescence emission originated from the lowest-lying $^1CT_{DA}$ state.[49,50] Intriguingly, ~1000 cm^{-1} (**TDBA-Ac**) and ~1400 cm^{-1} (**PzTDBA**) blue-shifted emissions were observed in PS doping films compared to in toluene (comparable polarity), indicating the presence of multifaceted interactions, which are discussed below.

The T_1 state of **TDBA-Ac** was identified as a local excited state on the acceptor (noted as ^3LE_A) while the T_1 excitation of **PzTDBA** was localized on the donor (^3LE_D), which allows direct $T_1 \rightarrow S_1$ RISC ($^3LE_{D/A} \rightarrow {}^1CT_{DA}$).[51,52] Meanwhile, the T_2 states of **TDBA-Ac** and **PzTDBA** were recognized as charge transfer states ($^3CT_{DA}$). With identical orbital wavefunction to the $^1CT_{DA}$ state, the corresponding $T_2 \rightarrow S_1$ RISC ($^3CT_{DA} \rightarrow {}^1CT_{DA}$) is forbidden.[51,52] By further confirming the CT/LE nature of low-lying singlet/triplet states through natural transition orbital (NTO) analysis (Fig. S4 and S5†) and hole–electron analysis (Table S4†),[53,54] the $T_1 \rightarrow S_1$ ($^3LE_{D/A} \rightarrow {}^1CT_{DA}$) transition was assigned as the accessible RISC channel that is responsible for the delayed fluorescence of **TDBA-Ac** and **PzTDBA**.

The thermally accessible ΔE_{ST} is critical for RISC, while estimating ΔE_{ST} through the vertical excitation energy of S_1 and T_1 states was reported to be unreliable.[55] Thus, we further optimized the S_1 and T_1 geometry of the **TDBA-Ac** and **PzTDBA** emitters to estimate adiabatic ΔE^*_{ST}. As listed in Table 1, **TDBA-Ac** and **PzTDBA** exhibit ΔE^*_{ST} of ~0.3 eV and ~0.26 eV in low-polarity media (CHX and TOL, $\Delta f < 0.02$), respectively, facilitating RISC for harvesting T_1 states with moderate $\langle S_1|\hat{H}_{SO}|T_1\rangle$. However, increasing to medium polarity (in DCM, $\Delta f = 0.22$) leads to enlarged ΔE^*_{ST} (>0.33 eV) for **TDBA-Ac** and **PzTDBA** with nearly unchanged $\langle T_1|\hat{H}_{SO}|S_1\rangle$, which might explain the reduced RISC rate (k_{RISC}). Note that the vertical (ΔE_{ST}) and adiabatic (ΔE^*_{ST}) singlet-triplet energy gap does not have a certain magnitude relationship as it depends on multiple factors, such as the different ES-SR in the S_1/T_1 states and steepness of the corresponding potential energy surface (PES), which are simplified as schematic diagrams (Fig. S6†). The total Φ_F and corresponding prompt/delayed (Φ_{PF}/Φ_{DF}) contribution of **TDBA-Ac** and **PzTDBA** were further measured in different solutions

Table 1 TDDFT calculated vertical (E) and adiabatic (E^*) excitation energy of the lowest-lying (S_1, T_1) states and corresponding energy gaps (ΔE_{ST}, ΔE^*_{ST}) of **TDBA-Ac** and **PzTDBA** in different mediums using PCM as the model; SOC matrix elements for ISC ($\langle S_1|\hat{H}_{SO}|T_1\rangle$) and RISC ($\langle T_1|\hat{H}_{SO}|S_1\rangle$) were calculated by using the linear response approach

	TDBA-Ac			**PzTDBA**		
	CHX	TOL	DCM	CHX	TOL	DCM
$E(S_1)$/eV	3.617	3.626	3.667	3.130	3.142	3.207
$E(T_1)$/eV	3.250	3.251	3.252	3.015	3.014	3.010
ΔE_{ST}/eV	0.367	0.375	0.415	0.115	0.128	0.197
$E^*(S_1)$/eV	3.474	3.482	3.509	2.792	2.804	2.861
$E^*(T_1)$/eV	3.173	3.173	3.174	2.539	2.538	2.531
ΔE^*_{ST}/eV	0.301	0.309	0.335	0.253	0.266	0.330
$\langle S_1\|\hat{H}_{SO}\|T_1\rangle$/$cm^{-1}$	0.338	0.339	0.294	0.016	0.018	0.058
$\langle T_1\|\hat{H}_{SO}\|S_1\rangle$/$cm^{-1}$	0.341	0.341	0.341	0.053	0.052	0.058

and PS doping films. As illustrated in Fig. 1c, **TDBA-Ac** exhibits nearly solvent-independent Φ_F (30–50%). With increasing solvent polarity, the solvation of the $^1CT_{DA}$ (S_1) state and unchanged energy level of the ^3LE_A (T_1) state resulted in reduced ΔE_{ST},[50,56] which is consistent with the observed increasing of the Φ_{DF} contribution (Φ_{DF}/Φ_F, Fig. 1c). Upon optical excitation, $S_1 \rightarrow T_1 \rightarrow S_1$ is the only feasible channel for delayed fluorescence,[17,38,57] and increased Φ_{DF}/Φ_F might correspond to higher Φ_{ISC} and Φ_{RISC}. In contrast, the Φ_F of **PzTDBA** rapidly decreased from 37% in non-polar CHX to undetectably low in polar mediums, which implies different relaxation of the photo-generated S_1 state. Intriguingly, **TDBA-Ac** and **PzTDBA** exhibit nearly 100% Φ_F and an evenly divided contribution of Φ_{PF} and Φ_{DF} ($\Phi_{DF}/\Phi_F \approx 50\%$) in PS doping films, indicating that the S_1 state decay is dominantly radiative, while all ISC-generated T_1 states can be harvested through subsequent RISC. Considering the importance of Φ_F, resolving the photophysics behind the fully radiative relaxation of orange–red **PzTDBA** in doping film would be of high interest.

tr-FL and excited-state relaxation

The time-resolved fluorescence (tr-FL) measurements of **TDBA-Ac** and **PzTDBA** were further performed by time-correlated single-photon counting (TCSPC) upon excitation at λ_{ex} = 400 nm.

The resulting traces were fitted as the sum of prompt (τ_{PF}) and delayed (τ_{DF}) components (Fig. S7, S8† and Table 2). Combining with measured Φ_{PF} and Φ_{DF}, the rate constants for ISC ($S_1 \rightarrow T_1$, k_{ISC}) and RISC ($T_1 \rightarrow S_1$, k_{RISC}) as well as corresponding Φ_{ISC} and Φ_{RISC} were estimated (Table 2). With calculated SOC matrix elements ($\langle S_1|\hat{H}_{SO}|T_1\rangle$ and $\langle T_1|\hat{H}_{SO}|S_1\rangle$), we attempted to reproduce the experimentally extracted values of k_{ISC} and k_{RISC} using the thermal vibration correlation function (TVCF)[16,54,58] and semi-classical Marcus[59,60] approaches. However, as shown in Table S5,† TVCF and Marcus approaches failed to describe k_{ISC} and k_{RISC}, which might be attributed to the ignorance of non-Condon effects, such as Herzberg–Teller coupling and spin–vibronic coupling.[61–63] Meanwhile, we noticed that calculation errors for the k_{ISC} of **PzTDBA** are much more significant than for **TDBA-Ac**, which might imply higher structural flexibility of **PzTDBA** and will be discussed in detail below. By further estimating the experimental values of k_R^S, k_{NR}^S and k_{NR}^T (Table 2), the quantitative contribution of the plausible relaxation channels was calculated for the S_1 and T_1 states.

As visualized in Fig. 2, the S_1 relaxation of **TDBA-Ac** is dominated by the slightly increased ISC with increased solvent polarity, while the ISC-generated T_1 states can be converted to S_1 with nearly identical Φ_{RISC}, which leads to the nearly unchanged Φ_F of **TDBA-Ac** in CHX (0.53), TOL (0.49) and DCM (0.47). In contrast, although ISC still dominates the S_1 decay of **PzTDBA** in CHX and TOL, the generated T_1 states largely decay non-radiatively to S_0 rather than thermally converting to S_1 *via* RISC, for which a low Φ_F was observed in CHX (0.37) and TOL (0.13). In high-polarity DCM, the S_1 decay of **PzTDBA** is predominately occupied by the non-radiative path to S_0, leading to an undetectable Φ_F (<0.01), which might be attributed to the exponentially increased k_{NR}^S described by band-gap law with the reducing of the $S_1 \rightarrow S_0$ energy gap ($\Delta E_{S_1-S_0}$).

Intriguingly, **TDBA-Ac** and **PzTDBA** exhibit nearly identical pattern of S_1 and T_1 decay in PS doping films, which is largely differed with observation in solutions. The S_1 decay of **TDBA-Ac** and **PzTDBA** in PS doping films are dominated by equally divided radiative decay ($S_1 \rightarrow S_0$) and ISC ($S_1 \rightarrow T_1$), while ISC-generated T_1 states can be further converted to S_1 through efficient RISC (Φ_{RISC} > 0.9). Due to negligible role of non-radiative path in both S_1 (<5%) and T_1 (<10%) state decay, **TDBA-Ac** and **PzTDBA** exhibit unexpectedly high Φ_F in PS doping films, which agrees with the reported high η_{EQE} of corresponding OLED devices.[45,46] However, such high Φ_F (0.95) of

Table 2 Measured photophysical data for the TDBA-Ac and PzTDBA emitters in N_2-saturated solutions and PS doping films

	TDBA-Ac				**PzTDBA**			
	[a]CHX	[a]TOL	[a]DCM	[b]PS	[a]CHX	[a]TOL	[a]DCM	[b]PS
τ_{PF}/ns	6.72	21.35	36.15	14.12	8.70	23.95	13.62	38.25
τ_{DF}/μs	0.15	0.14	0.48	1.21	0.10	0.29	0.23	1.10
Φ_F	0.53	0.49	0.47	0.90	0.37	0.13	<0.01	0.95
Φ_{PF}	0.23	0.16	0.11	0.44	0.03	0.03	<0.01	0.50
Φ_{DF}	0.30	0.33	0.36	0.46	0.34	0.10	0	0.45
[f]Φ_{ISC}	0.57	0.67	0.78	0.51	0.93	0.78	0	0.47
[g]Φ_{RISC}	0.39	0.39	0.43	0.82	0.35	0.10	0	0.90
[c]$k_{PF}/10^7$ s^{-1}	14.88	4.69	2.77	7.14	11.49	4.17	7.35	2.63
[d]$k_R^S/10^6$ s^{-1}	33.48	7.70	3.05	31.43	3.10	1.13	—	13.16
[e]$k_{NR}^S/10^6$ s^{-1}	30.29	7.82	3.16	3.49	5.28	8.02	73.46	0.69
[d]$k_{ISC}/10^7$ s^{-1}	8.50	3.14	2.15	3.65	10.66	3.25	—	1.25
[c]$k_{DF}/10^6$ s^{-1}	3.57	3.54	1.01	0.74	3.63	0.43	—	0.86
[d]$k_{RISC}/10^5$ s^{-1}	18.75	17.57	4.98	6.69	13.42	0.52	—	8.20
[d]$k_{NR}^T/10^5$ s^{-1}	31.50	32.55	9.60	4.49	35.91	4.24	—	4.53

[a] Concentration of 10^{-5} M. [b] Doping concentration of 2 wt%. [c] Calculated by $k_{PF} = 1/\tau_{PF}$ and $k_{DF} = 1/\tau_{DF}$. [d] Rate constants k_R^S, k_{ISC}, k_{RISC} and k_{NR}^T were calculated using the method described by Adachi *et al.*[10,19] [e] Calculated using $k_{NR}^S = k_{PF} - k_R^S - k_{ISC}$. [f] Calculated using $\Phi_{ISC} = k_{ISC}/(k_{ISC} + k_R^S + k_{NR}^S)$. [g] Calculated using $\Phi_{RISC} = \Phi_{DF}/(1 - \Phi_{PF})$.

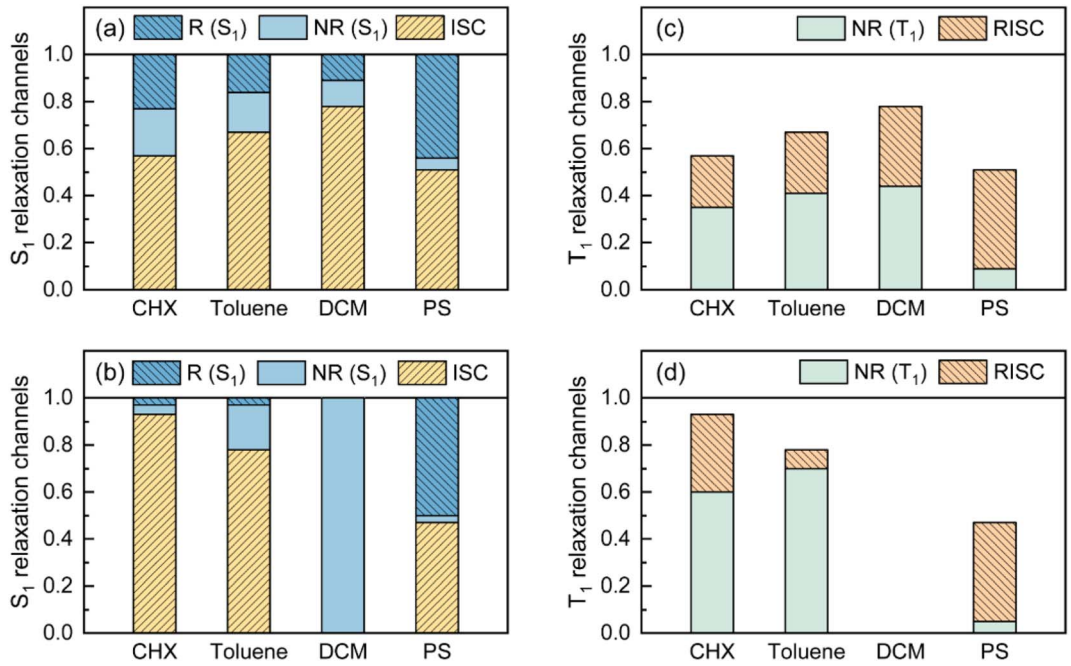

Fig. 2 Visualized contribution of ISC ($S_1 \rightarrow T_1$), radiative (R, $S_1 \rightarrow S_0$) and non-radiative (NR, $S_1 \rightarrow S_0$) decay of S_1 state for **TDBA-Ac** (a) and **PzTDBA** (b) in various solutions and PS doping films. Contribution of RISC ($T_1 \rightarrow S_1$) and non-radiative (NR, $T_1 \rightarrow S_0$) decay of T_1 state for **TDBA-Ac** (c) and **PzTDBA** (d) in various solutions and PS doping films, radiative decay of T_1 state was ignored due to low contribution.

PzTDBA observed in PS doping film seems to be inconsistent with the energy gap law, implying unique photophysics by which non-radiative decay of S_1 state can be greatly suppressed.

fs-TA and structural relaxation

The fs-TA signal upon UV excitation ($\lambda_{ex} = 320$ nm) of **TDBA-Ac** and **PzTDBA** in CHX solution and PS doping film were recorded by broadband probe ($\lambda_{probe} = 350$–750 nm) with delay times up to 7.0 ns, and the temporal resolution of fs-TA was measured to be ~90 fs. As shown in Fig. S9 and S10,† the measured fs-TA signals of **TDBA-Ac** and **PzTDBA** are contributed by negative ground-state bleaching (GSB) in the $\lambda_{probe} = 350$–400 nm regime, and the positive excited-state absorption (ESA) band extended in the longer wavelength region up to $\lambda_{probe} = 750$ nm.

Upon UV excitation, high-lying S_n states can be populated, followed by rapid internal conversion (IC, $S_n \rightarrow S_1$) to the long-lived S_1 state, which explains the dramatically reshaped ESA in the 1 ps delay time.[64,65] For the subsequent delay times of 1 ps to 1 ns, fs-TA evolution visualizes wavepacket motion that highly depends on the topology of S_1 PES.[41,66–68] For instance, the role of the excited-state structural relaxation (ES-SR) in the S_1 state decay of DA- and DAD/ADA-type TADF emitters has been intensively reported.[69–73] Suffering from the poor structural sensitivity of UV/Vis fs-TA, S_1/S_0 ES-SR usually leads to minimized alternation of the ESA shape, which is consistent with the observed fs-TA of **TDBA-Ac** and **PzTDBA** for 1 ps to 1 ns delay times.[41,74]

For characterizing S_1/S_0 ES-SR, the geometries of **TDBA-Ac** and **PzTDBA** in the S_0, S_1 and T_1 states were optimized using DFT and TD-DFT approaches. The resulting structures are illustrated in Table S6,† while total reorganization energies ($\lambda_{S_0 \rightarrow S_1}$ and $\lambda_{S_1 \rightarrow S_0}$) were calculated for evaluating the ES-SR of the **TDBA-Ac** and **PzTDBA** emitters together with the root of the mean squared displacement ($RMSD_{S_1/S_0}$) between the S_0 and S_1 states (Fig. S11†). As listed in Table 3, the calculated values of $\lambda_{S_0 \rightarrow S_1}$, $\lambda_{S_1 \rightarrow S_0}$ and $RMSD_{S_1/S_0}$ indicate a more pronounced ES-ER of **PzTDBA** in the S_1 state than **TDBA-Ac**, which obviously cannot be attributed to structural extension (DA to ADA structure) as the total reorganization energy and RMSD are not additive. To evaluate the contribution of each of the molecular fragments of the **TDBA-Ac** and **PzTDBA** emitters to the ES-SR, several critical structural parameters were defined, as illustrated in Fig. S12† and measured (Table 3) for the S_0 and S_1 states. Upon vertical excitation, **TDBA-Ac** and **PzTDBA** initially remain in S_0 geometry in the Franck–Condon (FC) region, following by ES-SR until reaching the global minimum of S_1 PES, *i.e.* optimized S_1 geometry. For **TDBA-Ac**, S_1/S_0 ES-SR featured a slight increase in the D–A twisting angle β from 89.82° (S_1^{FC}) to 92.00° (S_1^{T}), while the dihedral angles of the Ac (α) and TDBA (γ) framework bending remained nearly unchanged in the S_1 state decay. In contrast, ADA-type **PzTDBA** exhibits higher flexibility than that of **TDBA-Ac**. In addition to the fast motion of the D–A twisting angle (β) from 79.72°/79.06° (S_1^{FC}) to 89.02°/91.43° (S_1^{T}), framework planarization of the center donor (Pz) was observed as the dihedral angle (α) increased from 164.57° (S_1^{T}) to 180.00° (S_1^{TP}). The simultaneous S_0–S_1 state changing of α and β angles may correspond to a two-step S_1/S_0 ES-SR ($S_1^{FC} \rightarrow S_1^{T} \rightarrow S_1^{TP}$), which has been widely reported,[75,76] *i.e.* fast D–A twisting ($S_1^{FC} \rightarrow S_1^{T}$) followed by slow framework planarization ($S_1^{T} \rightarrow S_1^{TP}$). Target analysis was further performed to acquire

Table 3 DFT and TD-DFT (M06-2X, 6-311G**, PCM = toluene) calculated optimal geometric parameters of **TDBA-Ac** and **PzTDBA** in the S_0, S_1 and T_1 states, as well as the calculated total reorganization energy and RMSD associated with the S_1 state ES-SR[a]

	TDBA-Ac			**PzTDBA**		
	*α (°)	**β (°)	***γ (°)	*α (°)	**β_1/β_2 (°)	***γ_1/γ_2 (°)
S_0 geometry	176.50	89.82	11.36	164.57	79.72/79.06	11.56/10.99
S_1 geometry	175.45	92.00	12.12	180.00	89.02/91.43	11.65/11.37
T_1 geometry	176.57	90.82	4.77	180.00	88.60/91.33	11.40/11.40
$\lambda_{S_0 \rightarrow S_1}$ (cm^{-1})	1161			2790		
$\lambda_{S_1 \rightarrow S_0}$ (cm^{-1})	1273			2552		
$RMSD_{S_1/S_0}$ (Å)	0.053			0.241		

[a] *Bending dihedral angle of donor (Ac/Pz); **donor–acceptor twisting angle; ***bending dihedral angle of acceptor (TDBA).

quantitative information on S_1/S_0 ES-SR that may play a key role in the S_1 state relaxation. By including three or four sequential decay processes, measured fs-TA data can be well-reproduced by the displayed decay-associated spectra (DAS) of each decay components and concentration evolution of each transient species (Fig. 3), while species-associated spectra (SAS) can be seen in Fig. S13 and S14.†

The initial decay (A → B) with 300–400 fs time constant was accompanied by considerable ESA reshaping, corresponding to rapid IC ($S_n \rightarrow S_1$). The fs-TA was subsequently dominated by S_1/S_0 ES-SR until the wavepacket reached the global minimum of S_1 PES. For **PzTDBA**, highlighted two-step S_1/S_0 ES-SR (B → C → D, *i.e.* $S_1^{FC} \rightarrow S_1^{T} \rightarrow S_1^{TP}$) predicted by calculated S_0 and S_1 geometries was observed, featuring a slight ESA reshaping. The

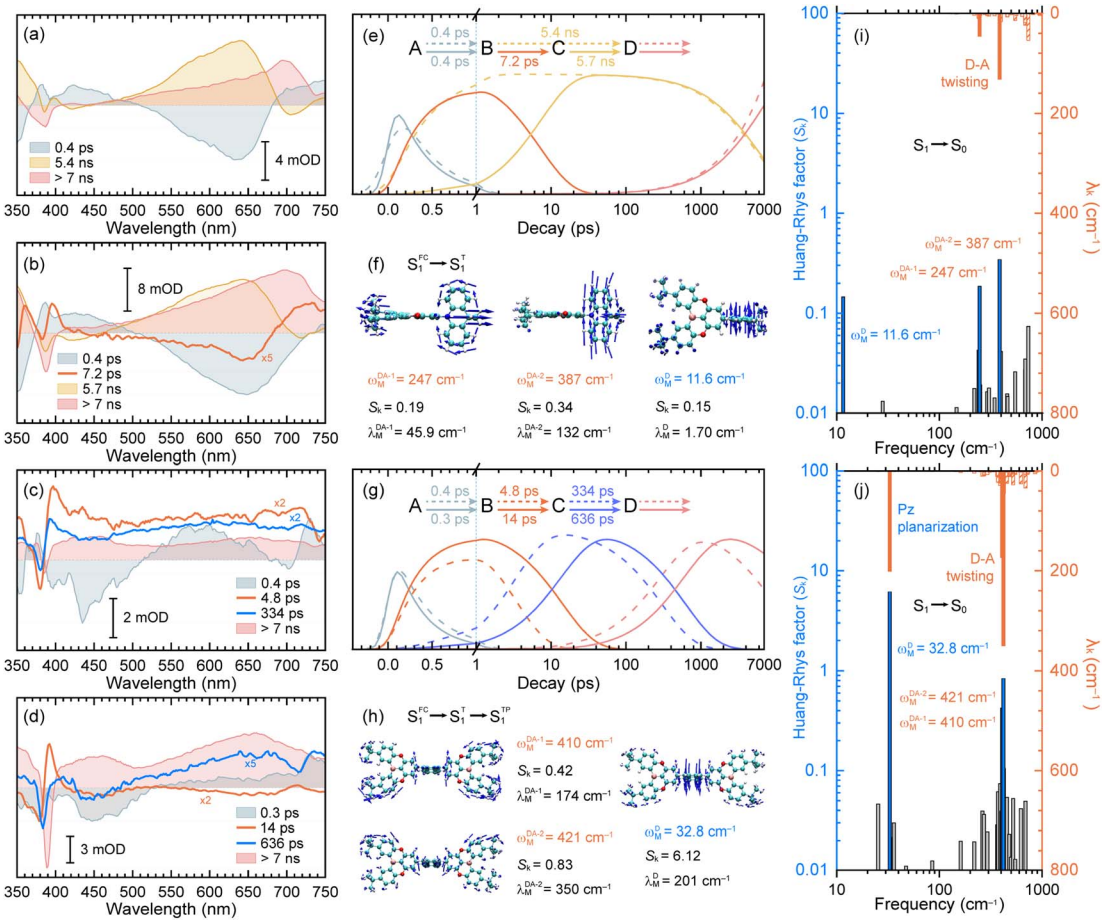

Fig. 3 The decay-associated spectra (DAS) extracted from the fs-TA data of **TDBA-Ac** in CHX solution (a) and PS doping film (b) as well as **PzTDBA** in CHX solution (c) and PS doping film (d). Fitted concentration evolution of **TDBA-Ac** (e) and **PzTDBA** (g) in CHX solution (dashed lines) and PS doping film (solid lines). Promoting vibrational modes of **TDBA-Ac** (f) and **PzTDBA** (h) with large contribution to the HR factors. Calculated HR factors and reorganization energy contribution of each vibrational mode of **TDBA-Ac** (i) and **PzTDBA** (j) for the $S_1 \rightarrow S_0$ transition in CHX solution. The dominant modes displayed in (f) and (h) are highlighted correspondingly.

observed fast (4.8 ps in CHX, $S_1^{FC} \rightarrow S_1^{T}$) and slow (334 ps in CHX, $S_1^{T} \rightarrow S_1^{TP}$) steps correspond to D–A twisting (β_1/β_2 angles) and Pz planarization (α angle), respectively.

For **TDBA-Ac**, one-step S_1/S_0 ES-SR was observed (7.2 ps, $S_1^{FC} \rightarrow S_1^{T}$) in the PS doping film, corresponding to the D–A twisting (β angle), which is comparable with the fast S_1/S_0 ES-SR step of **PzTDBA**. However, S_1/S_0 ES-SR of **TDBA-Ac** was unobservable in CHX, which might be attributed to a less pronounced $S_0 \rightarrow S_1$ structural change than for **PzTDBA**, *i.e.* nearly unchanged β angle in the S_0 (89.82°) and S_1 (92.00°) states.

Intriguingly, the extracted time constants of D–A twisting ($S_1^{FC} \rightarrow S_1^{T}$, 14.0 ps) and Pz planarization ($S_1^{T} \rightarrow S_1^{TP}$, 636 ps) of **PzTDBA** in the PS doping film are 2–3 times slower than corresponding S_1/S_0 ES-SR steps in CHX (Fig. 3g and S15†), implying a higher potential barrier for S_1 PES, which is consistent with our fs-TA observations for multiple-resonance emitters.[77] Moreover, slow S_1 isomerization of azo-benzene embedded in polymer films was reported previously, attributing to external structural restraint from polymer micro-networks.[78]

As discussed above, the fluorescence emission of **PzTDBA** was strongly quenched ($\Phi_F = 0.37$ in CHX) in solutions due to the presence of fast non-radiative decay, while a high Φ_F (>0.95) in the PS doping film may be feasible if non-radiative $S_1 \rightarrow S_0$ decay can be greatly suppressed. Our fs-TA data revealed higher S_1/S_0 ES-SR barriers of **PzTDBA** in PS doping films than in CHX, which might imply the presence of an underlying association between S_1/S_0 ES-SR and the non-radiative decay of the S_1 state, *i.e.* restrained S_1/S_0 ES-SR leads to suppressed non-radiative decay. Conversely, k_{NR}^{S} was described to be highly correlated with promoting vibrational modes by the energy gap law (eqn (5)).[21,23] Thus, we attempted to unveil the underlying relationship among the S_1/S_0 ES-SR, promoting modes and non-radiative decay of the S_1 state.

Vibrational analysis and non-radiative decay

The energy gap law (eqn (5)) clearly describes how promoting vibrational modes affect k_{NR}^{S} through their vibrational frequency (ω_M) and reorganization energy (λ_M), while promoting modes are vibrational modes that are considerably involved in the EVC of the S_1 state through a pronounced Huang-Rhys (HR) factor (S_k).[24,79,80] We further calculated the S_k and λ_k contribution of each of the vibrational modes involved in the $S_1 \rightarrow S_0$ transition (Fig. 3i and j), in which the promoting modes associated with the k_{NR}^{S} of **TDBA-Ac** and **PzTDBA** are illustrated in Fig. 3f and h, respectively.

As shown in Fig. 3j and h, three promoting modes were identified for the $S_1 \rightarrow S_0$ transition of **PzTDBA** due to considerable S_k. The modes at 410 cm^{-1} ($\omega_M^{DA\text{-}1}$) and 421 cm^{-1} ($\omega^{DA\text{-}2}{}_M$) correspond to symmetric and asymmetric D–A twisting and exhibit considerable reorganization energy contributions ($\lambda^{DA\text{-}1}{}_M = 174$ cm^{-1} and $\lambda_M^{DA\text{-}2} = 350$ cm^{-1}), which are associated with the fast S_1/S_0 ES-SR step observed on fs-TA of **PzTDBA**, *i.e.* $S_1^{FC} \rightarrow S_1^{T}$ with the D–A twisting motion. For **TDBA-Ac** (Fig. 3i and f), the corresponding S_1/S_0 ES-SR of D–A twisting is associated with promoting modes at $\omega_M^{DA\text{-}1} = 247$ cm^{-1} and $\omega_M^{DA\text{-}2} = 387$ cm^{-1} with substantially lower $\lambda_M^{DA\text{-}1}$ (45.9 cm^{-1}) and $\lambda_M^{DA\text{-}2}$ (132 cm^{-1}), which is consistent with its rigid structure predicted theoretically, *i.e.* less pronounced S_1/S_0 ES-SR than **PzTDBA**.

Meanwhile, $S_1 \rightarrow S_0$ decay of **PzTDBA** features a promoting mode at $\omega_M^{D} = 32.8$ cm^{-1} with a surprisingly high HR factor ($S_k = 6.12$) and considerable reorganization energy ($\lambda_M^{D} = 201.1$ cm^{-1}), corresponding to the bending motion of the Pz framework, which is clearly associated with the observed slow S_1/S_0 ES-SR step of **PzTDBA**, *i.e.* $S_1^{T} \rightarrow S_1^{TP}$. Intriguingly, this particular mode was also observed for **TDBA-Ac** at $\omega_M^{D} = 11.6$ cm^{-1} with a much lower HR factor ($S_k = 0.15$) and a two orders of magnitude lower reorganization energy contribution ($\lambda_M^{D} = 1.70$ cm^{-1}) than that of **PzTDBA**, indicating that it was excluded from the $S_1 \rightarrow S_0$ decay of **TDBA-Ac**. As a result, the second S_1/S_0 ES-SR step ($S_1^{T} \rightarrow S_1^{TP}$) was absent from the fs-TA signal of **TDBA-Ac**.

Furthermore, we investigated the influence of medium polarity on the promoting modes of the **TDBA-Ac** and **PzTDBA** emitters. As shown in Fig. S16,† for **PzTDBA** in DCM solution, an extra promoting mode at 15.4 cm^{-1} was observed with considerable S_k but ignorable λ_k, which might be less associated with the non-radiative decay of S_1 state **PzTDBA**. In contrast, a promoting mode at 12.4 cm^{-1} was observed for **TDBA-Ac** with considerable S_k (8.71) and λ_k (108.23 cm^{-1}) in DCM solution, which is very different from the case of **TDBA-Ac** in low-polarity solvents, indicating that the S_1/S_0 ES-SR of **TDBA-Ac** (DA-type) is more evidentially coupled with charge transfer than **PzTDBA** (ADA-type).

As discussed above, the one- (**TDBA-Ac**, $S_1^{FC} \rightarrow S_1^{T}$) and two-step (**PzTDBA**, $S_1^{T} \rightarrow S_1^{TP}$) S_1/S_0 ES-SR are directly associated with promoting vibrational modes that are considerably involved in the EVC of the S_1 state through their HR factor. Meanwhile, promoting modes contribute to the k_{NR}^{S} of the S_1 state through corresponding λ_M, which implies that S_1/S_0 ES-SR can significantly affect k_{NR}^{S} (and subsequently Φ_F) through the promoting vibrational modes (Fig. 4). For instance, the one-step S_1/S_0 ES-SR of **TDBA-Ac** is associated with vibrational modes with low S_k and λ_M, while the promoting modes associated with the two-step S_1/S_0 ES-SR of **PzTDBA** have much higher S_k and λ_M. As a result, the non-radiative channel plays a minor role in the S_1 decay of structurally rigid **TDBA-Ac**, while the emission of structurally flexible **PzTDBA** is severely hampered by the fast non-radiative decay of the S_1 state. Furthermore, the two-step S_1/S_0 ES-SR motions of **PzTDBA** are greatly suppressed in the PS doping films due to the external structural restraint, for which the S_1 non-radiative decay associated with the promoting modes might be correspondingly weakened, leading to the greatly improved Φ_F of **PzTDBA** in the doping films. In this sense, the external structural restraint for S_1/S_0 ES-SR motions might be critical for achieving a high η_{EQE} for TADF-based OLED devices.

To directly verify the influence of the external structural restraint on the S_1 non-radiative decay of **PzTDBA**, we measured temperature-dependent emission spectra of **PzTDBA** in polyethylene oxide (PEO) doping films (Fig. S18†). With a glass transition temperature (T_g) of 220 K, PEO provides a "softer"

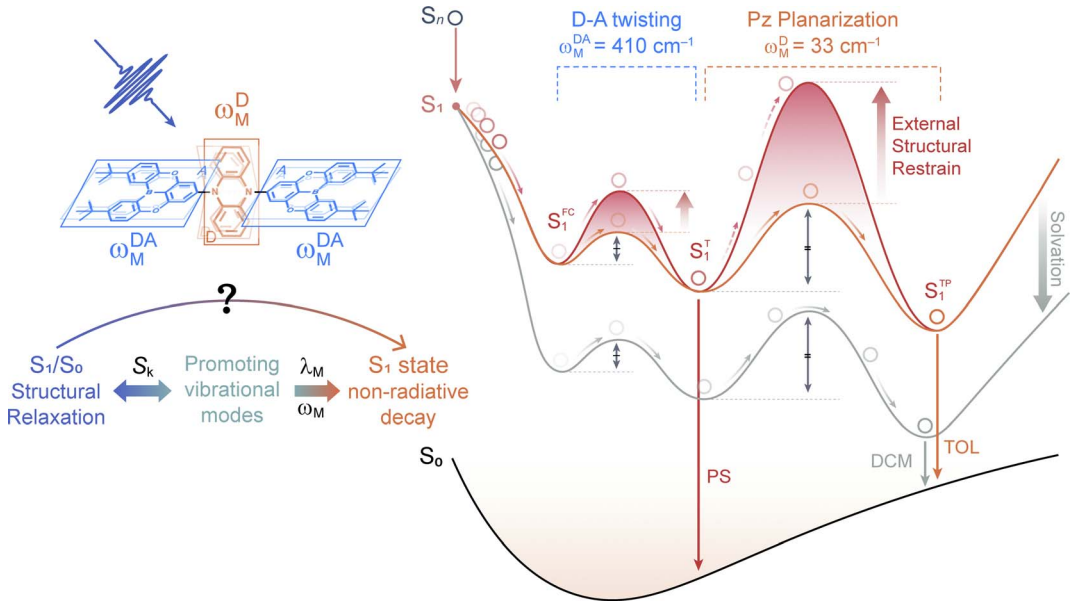

Fig. 4 Simplified energetic diagram illustrating two-step ES-SR ($S_1^{FC} \rightarrow S_1^{T}$ and $S_1^{T} \rightarrow S_1^{TP}$) of **PzTDBA** in low-polarity solution (orange line, TOL), high-polarity solution (cyan line, DCM) and PS doping film (red line). The double arrows represent the potential barriers of D–A twisting ($S_1^{FC} \rightarrow S_1^{T}$) and Pz planarization ($S_1^{T} \rightarrow S_1^{TP}$).

microenvironment than PS (T_g = 373 K) and can be further "softened" by increasing the temperature.[81,82] As a TADF emitter, **PzTDBA** was expected to be more fluorescent at higher temperatures due to faster RISC. However, we observed clear fluorescence quenching with increasing temperature in the 297–347 K range, indicating that non-radiative decay was enhanced in the medium with reduced external structural restraint, which is consistent with our analysis described above.

Note that we cannot perform vibrational analysis for TADF emitters with the presence of the external structural restraint, but we speculate that the λ_M of the promoting modes of **PzTDBA** might be greatly reduced due to the external structural restraint, in agreement with slowed S_1/S_0 ES-SR motions in the doping films, especially the Pz bending mode (ω_M^D) associated with the slow S_1/S_0 ES-SR step ($S_1^T \rightarrow S_1^{TP}$) might be terminated. As a result, S_1^T instead of S_1^{TP} might dominate the emission of **PzTDBA** in the PS doping films (see Fig. 4), which explains the observed blue-shifted emission in the PS doping film compared with the case in toluene solution, which has comparable polarity to the PS medium. Meanwhile, the emission of **PzTDBA** in solutions mainly originates from S_1^{TP} due to the accessible barrier of $S_1^T \rightarrow S_1^{TP}$, which thus suffers from the plague of non-radiative decay (Fig. 4).

Last but not least, in addition to the S_1 state, we noticed that **TDBA-Ac** and **PzTDBA** exhibit a suppressed non-radiative decay channel of the T_1 state in the PS doping films compared to in solutions (Fig. 2c and d), which inspired us to consider the role of T_1/S_0 ES-SR in the non-radiative decay of the T_1 state. As shown in Fig. S17,† **TDBA-Ac** exhibits several vibrational modes with considerable S_k in the region <100 cm^{-1}, but the low λ_M implies that ES-SR may not be strongly associated with non-radiative $T_1 \rightarrow S_0$ decay. In contrast, the promoting modes of **PzTDBA** at 32.9 cm^{-1} and 421/410 cm^{-1} contribute considerable λ_M, while pronounced T_1/S_0 ES-SR was indicated (Table 3), including Pz bending and D–A twisting. Therefore, it might be plausible that the non-radiative $T_1 \rightarrow S_0$ decay is similarly associated with two T_1/S_0 ES-SR motions, because the non-radiative $T_1 \rightarrow S_0$ decay of **PzTDBA** was strongly suppressed in the PS doping film due to the external structural restraint. However, unlike S_1 relaxation, without direct spectroscopic evidence of T_1/S_0 ES-SR in different media, verifying this hypothesis requires further investigation.

Conclusions

To summarize, we performed a comprehensive investigation of the photophysics of two TADF emitters, **TDBA-Ac** (DA-type, blue light) and **PzTDBA** (ADA-type, orange–red light), using fs-TA, tr-FL and theoretical approaches. Compared with the one-step S_1/S_0 ES-SR ($S_1^{FC} \rightarrow S_1^{T}$) of **TDBA-Ac**, the S_1 state decay of **PzTDBA** is dominated by two steps, S_1/S_0 ES-SR ($S_1^{FC} \rightarrow S_1^{T} \rightarrow S_1^{TP}$), while greatly slowed S_1/S_0 ES-SR motions of **PzTDBA** were observed in the PS doping films due to the external structural restraints. Vibrational analysis indicated that the S_1/S_0 ES-SR motions are directly associated with the promoting modes that are considerably involved in the EVC of the S_1 state through their own S_k, while the promoting modes contribute to fast k_{NR}^S *via* λ_M. In doping films, the external structural restraint leads to suppressed S_1/S_0 ES-SR and reorganization energy contribution of the promoting modes, resulting in slowed k_{NR}^S and a highly fluorescent S_1 state that is favorable for OLED application. With **TDBA-Ac** and **PzTDBA** as model systems, we established the connection among the S_0/S_1 ES-SR, promoting modes and k_{NR}^S of TADF emitters, which indicated the key role of the external

structural restraint in obtaining high Φ_F TADF emitters. Our work also provides a new direction for OLED design, and it might be necessary to take the rigidity of host materials used for the emitting layer into consideration to avoid emission quenching through fast non-radiative decay associated with the S_1/S_0 ES-SR of TADF emitters, especially for TADF emitters with a relatively small band gap, which might be a useful reference for future OLED application.

Data availability

All experimental and calculational data are available from the corresponding author upon reasonable request.

Author contributions

Yixuan Gao: conceptualization, methodology, investigation, data curation, formal analysis, visualization, and writing – original draft; Yaxin Wang: methodology, data curation, formal analysis, and validation; Zilong Guo: investigation, visualization, project administration, and supervision; Yan Wan: methodology and resources; Zheng Xue and Yandong Han: resources and project administration; Wensheng Yang: supervision, resources, and funding acquisition; Xiaonan Ma: conceptualization, formal analysis, funding acquisition, supervision, and writing – review and editing.

Conflicts of interest

The authors declare no competing financial interest.

Acknowledgements

We acknowledge the financial support from the National Key Research & Development Program of China (Grant No. 2020YFA0714603 and 2020YFA0714604). We thank Dr Yingli Niu (Beijing Jiaotong University) for his useful tutoring on MOMAP calculation and Dr Lei Zhou (HORIBA Scientific, Beijing) for valuable discussion on tr-FL measurements.

Notes and references

1 Y.-Z. Shi, H. Wu, K. Wang, J. Yu, X.-M. Ou and X.-H. Zhang, *Chem. Sci.*, 2022, **13**, 3625–3651.
2 Y. Huang, E.-L. Hsiang, M.-Y. Deng and S.-T. Wu, *Light: Sci. Appl.*, 2020, **9**, 105.
3 Z. Yang, Z. Mao, Z. Xie, Y. Zhang, S. Liu, J. Zhao, J. Xu, Z. Chi and M. P. Aldred, *Chem. Soc. Rev.*, 2017, **46**, 915–1016.
4 G. Hong, X. Gan, C. Leonhardt, Z. Zhang, J. Seibert, J. M. Busch and S. Bräse, *Adv. Mater.*, 2021, **33**, 2005630.
5 H.-W. Chen, J.-H. Lee, B.-Y. Lin, S. Chen and S.-T. Wu, *Light: Sci. Appl.*, 2017, **7**, 17168.
6 M. A. Baldo, D. F. O'Brien, Y. You, A. Shoustikov, S. Sibley, M. E. Thompson and S. R. Forrest, *Nature*, 1998, **395**, 151–154.
7 K. Goushi, K. Yoshida, K. Sato and C. Adachi, *Nat. Photonics*, 2012, **6**, 253–258.
8 L. J. Rothberg and A. J. Lovinger, *J. Mater. Res.*, 1996, **11**, 3174–3187.
9 M. Pope, H. P. Kallmann and P. Magnante, *J. Chem. Phys.*, 1963, **38**, 2042–2043.
10 Q. Zhang, B. Li, S. Huang, H. Nomura, H. Tanaka and C. Adachi, *Nat. Photonics*, 2014, **8**, 326–332.
11 H. Noda, H. Nakanotani and C. Adachi, *Sci. Adv.*, 2018, **4**, eaao6910.
12 H. Uoyama, K. Goushi, K. Shizu, H. Nomura and C. Adachi, *Nature*, 2012, **492**, 234–238.
13 J. M. Kaminski, A. Rodríguez-Serrano, F. Dinkelbach, H. Miranda-Salinas, A. P. Monkman and C. M. Marian, *Chem. Sci.*, 2022, **13**, 7057–7066.
14 H. Noda, X.-K. Chen, H. Nakanotani, T. Hosokai, M. Miyajima, N. Notsuka, Y. Kashima, J.-L. Brédas and C. Adachi, *Nat. Mater.*, 2019, **18**, 1084–1090.
15 M. Cai, M. Auffray, D. Zhang, Y. Zhang, R. Nagata, Z. Lin, X. Tang, C.-Y. Chan, Y.-T. Lee, T. Huang, X. Song, Y. Tsuchiya, C. Adachi and L. Duan, *Chem. Eng. J.*, 2021, **420**, 127591.
16 Q. Peng, D. Fan, R. Duan, Y. Yi, Y. Niu, D. Wang and Z. Shuai, *J. Phys. Chem. C*, 2017, **121**, 13448–13456.
17 T. Hosokai, H. Matsuzaki, H. Nakanotani, K. Tokumaru, T. Tsutsui, A. Furube, K. Nasu, H. Nomura, M. Yahiro and C. Adachi, *Sci. Adv.*, 2017, **3**, e1603282.
18 K. R. Naveen, P. Palanisamy, M. Y. Chae and J. H. Kwon, *Chem. Commun.*, 2023, **59**, 3685–3702.
19 Q. Zhang, H. Kuwabara, W. J. Potscavage, S. Huang, Y. Hatae, T. Shibata and C. Adachi, *J. Am. Chem. Soc.*, 2014, **136**, 18070–18081.
20 Z. Kuang, G. He, H. Song, X. Wang, Z. Hu, H. Sun, Y. Wan, Q. Guo and A. Xia, *J. Phys. Chem. C*, 2018, **122**, 3727–3737.
21 J. A. Treadway, B. Loeb, R. Lopez, P. A. Anderson, F. R. Keene and T. J. Meyer, *Inorg. Chem.*, 1996, **35**, 2242–2246.
22 T. Ogiwara, Y. Wakikawa and T. Ikoma, *J. Phys. Chem. A*, 2015, **119**, 3415–3418.
23 R. Englman and J. Jortner, *Mol. Phys.*, 1970, **18**, 145–164.
24 Y.-C. Wei, S. F. Wang, Y. Hu, L.-S. Liao, D.-G. Chen, K.-H. Chang, C.-W. Wang, S.-H. Liu, W.-H. Chan, J.-L. Liao, W.-Y. Hung, T.-H. Wang, P.-T. Chen, H.-F. Hsu, Y. Chi and P.-T. Chou, *Nat. Photonics*, 2020, **14**, 570–577.
25 C. E. Whittle, J. A. Weinstein, M. W. George and K. S. Schanze, *Inorg. Chem.*, 2001, **40**, 4053–4062.
26 J. S. Wilson, N. Chawdhury, M. R. A. Al-Mandhary, M. Younus, M. S. Khan, P. R. Raithby, A. Köhler and R. H. Friend, *J. Am. Chem. Soc.*, 2001, **123**, 9412–9417.
27 J. V. Caspar and T. J. Meyer, *J. Phys. Chem.*, 1983, **87**, 952–957.
28 Y. Xiao, H. Wang, Z. Xie, M. Shen, R. Huang, Y. Miao, G. Liu, T. Yu and W. Huang, *Chem. Sci.*, 2022, **13**, 8906–8923.
29 Y. Liu, X. Xiao, Y. Ran, Z. Bin and J. You, *Chem. Sci.*, 2021, **12**, 9408–9412.
30 C. Wang, X. Li, Y. Gao, L. Wang, S. Zhang, L. Zhao, P. Lu, B. Yang, S. Su and Y. Ma, *Adv. Opt. Mater.*, 2017, **5**, 1700441.
31 A. Abdurahman, Y. Chen, X. Ai, O. Ablikim, Y. Gao, S. Dong, B. Li, B. Yang, M. Zhang and F. Li, *J. Mater. Chem. C*, 2018, **6**, 11248–11254.

32 T.-L. Wu, M.-J. Huang, C.-C. Lin, P.-Y. Huang, T.-Y. Chou, R.-W. Chen-Cheng, H.-W. Lin, R.-S. Liu and C.-H. Cheng, *Nat. Photonics*, 2018, **12**, 235–240.
33 H. J. Kim, H. Kang, J. Jeong, S. H. Park, C. W. Koh, C. W. Kim, H. Y. Woo, M. J. Cho, S. Park and D. H. Choi, *Adv. Funct. Mater.*, 2021, **31**, 2102588.
34 X. Tang, Q. Bai, T. Shan, J. Li, Y. Gao, F. Liu, H. Liu, Q. Peng, B. Yang, F. Li and P. Lu, *Adv. Funct. Mater.*, 2018, **28**, 1705813.
35 S. Sharma and A. K. Pal, *J. Mater. Chem. C*, 2022, **10**, 15681–15707.
36 G. Chen, J. R. Swartzfager and J. B. Asbury, *J. Am. Chem. Soc.*, 2023, **145**, 25495–25504.
37 Y. Liu, J. Yang, Z. Mao, Y. Wang, J. Zhao, S.-J. Su and Z. Chi, *Chem. Sci.*, 2023, **14**, 1551–1556.
38 Y. Liu, C. Li, Z. Ren, S. Yan and M. R. Bryce, *Nat. Rev. Mater.*, 2018, **3**, 18020.
39 J. Xu, Y. Dai, J. Zhang, Z. Jia, Q. Meng and J. Qiao, *Adv. Opt. Mater.*, 2023, 2300989.
40 Z. Li, J.-R. Zhang, X.-K. Tian, S. Yang, S. Chen, H. Zhou and X.-G. Yang, *Chem. Sci.*, 2022, **13**, 9381–9386.
41 W. Zhang, H. Song, J. Kong, Z. Kuang, M. Li, Q. Guo, C. Chen and A. Xia, *J. Phys. Chem. C*, 2019, **123**, 19322–19332.
42 H. Miranda-Salinas, A. Rodriguez-Serrano, J. M. Kaminski, F. Dinkelbach, N. Hiromichi, Y. Kusakabe, H. Kaji, C. M. Marian and A. P. Monkman, *J. Phys. Chem. C*, 2023, **127**, 8607–8617.
43 T. Yang, B. Liang, Z. Cheng, C. Li, G. Lu and Y. Wang, *J. Phys. Chem. C*, 2019, **123**, 18585–18592.
44 J.-L. He, Y. Tang, K. Zhang, Y. Zhao, Y.-C. Lin, C.-K. Hsu, C.-H. Chen, T.-L. Chiu, J.-H. Lee, C.-K. Wang, C.-C. Wu and J. Fan, *Mater. Horiz.*, 2022, **9**, 772–779.
45 D. Karthik, Y. H. Jung, H. Lee, S. Hwang, B. Seo, J. Kim, C. W. Han and J. H. Kwon, *Adv. Mater.*, 2021, **33**, 2007724.
46 D. H. Ahn, S. W. Kim, H. Lee, I. J. Ko, D. Karthik, J. Y. Lee and J. H. Kwon, *Nat. Photonics*, 2019, **13**, 540–546.
47 P. J. B. Clarricoats, *Proc. IEE-Part C Monogr.*, 1962, **109**, 401.
48 Z. Tang, C. Chang, F. Bao, L. Tian, H. Liu, M. Wang, C. Zhu and J. Xu, *Polymers*, 2021, **13**, 284.
49 X. Niu, P. Gautam, Z. Kuang, C. P. Yu, Y. Guo, H. Song, Q. Guo, J. M. W. Chan and A. Xia, *Phys. Chem. Chem. Phys.*, 2019, **21**, 17323–17331.
50 W. Zhang, J. Kong, D. Hu, M. Tao, X. Niu, S. Vdović, D. Aumiler, Y. Ma and A. Xia, *J. Phys. Chem. C*, 2020, **124**, 5574–5582.
51 M. K. Etherington, J. Gibson, H. F. Higginbotham, T. J. Penfold and A. P. Monkman, *Nat. Commun.*, 2016, **7**, 13680.
52 J. Gibson, A. P. Monkman and T. J. Penfold, *ChemPhysChem*, 2016, **17**, 2956–2961.
53 Y. Wang, Z. Guo, Y. Gao, Y. Tian, Y. Deng, X. Ma and W. Yang, *J. Phys. Chem. Lett.*, 2022, **13**, 6664–6673.
54 Y. Wang, Y. Tian, Y. Gao, Z. Guo, Z. Xue, Y. Han, W. Yang and X. Ma, *J. Phys. Chem. Lett.*, 2023, **14**, 9665–9676.
55 H. Sun, C. Zhong and J.-L. Brédas, *J. Chem. Theory Comput.*, 2015, **11**, 3851–3858.
56 X. Zhao and J. Zhao, *Chem. Commun.*, 2022, **58**, 7666–7669.
57 H. Noda, H. Nakanotani and C. Adachi, *Chem. Lett.*, 2019, **48**, 126–129.
58 Q. Ou, Y. Shao and Z. Shuai, *J. Am. Chem. Soc.*, 2021, **143**, 17786–17792.
59 N. Aizawa, Y. Harabuchi, S. Maeda and Y.-J. Pu, *Nat. Commun.*, 2020, **11**, 3909.
60 Y. Olivier, B. Yurash, L. Muccioli, G. D'Avino, O. Mikhnenko, J. C. Sancho-García, C. Adachi, T.-Q. Nguyen and D. Beljonne, *Phys. Rev. Mater.*, 2017, **1**, 075602.
61 S. Lin, Z. Pei, B. Zhang, H. Ma and W. Liang, *J. Phys. Chem. A*, 2022, **126**, 239–248.
62 J. Tatchen, N. Gilka and C. M. Marian, *Phys. Chem. Chem. Phys.*, 2007, **9**, 5209.
63 B. R. Henry and W. Siebrand, *J. Chem. Phys.*, 1971, **54**, 1072–1085.
64 K. A. Zachariasse, M. Grobys, I. Riickert and W. Kiihnle, *J. Photochem. Photobiol., A*, 1997, **105**, 373–383.
65 M. C. Drummer, R. B. Weerasooriya, N. Gupta, B. T. Phelan, A. J. S. Valentine, A. A. Cordones, X. Li, L. X. Chen and K. D. Glusac, *J. Phys. Chem. C*, 2022, **126**, 1946–1957.
66 T. Bolze, J. Wree, F. Kanal, D. Schleier and P. Nuernberger, *ChemPhysChem*, 2018, **19**, 138–147.
67 H. Song, H. Zhao, Y. Guo, A. M. Philip, Q. Guo, M. Hariharan and A. Xia, *J. Phys. Chem. C*, 2020, **124**, 237–245.
68 J. Köhler, T. Quast, J. Buback, I. Fischer, T. Brixner, P. Nuernberger, B. Geiß, J. Mager and C. Lambert, *Phys. Chem. Chem. Phys.*, 2012, **14**, 11081.
69 Y. Rout, C. Montanari, E. Pasciucco, R. Misra and B. Carlotti, *J. Am. Chem. Soc.*, 2021, **143**, 9933–9943.
70 Z. Zhang, Y.-S. Wu, K.-C. Tang, C.-L. Chen, J.-W. Ho, J. Su, H. Tian and P.-T. Chou, *J. Am. Chem. Soc.*, 2015, **137**, 8509–8520.
71 Y. Chen, K.-H. Chang, F.-Y. Meng, S.-M. Tseng and P.-T. Chou, *Angew. Chem., Int. Ed.*, 2021, **60**, 7205–7212.
72 Z. Ma, Z. Yang, L. Mu, L. Deng, L. Chen, B. Wang, X. Qiao, D. Hu, B. Yang, D. Ma, J. Peng and Y. Ma, *Chem. Sci.*, 2021, **12**, 14808–14814.
73 Y. Wen, S. Xiao, H. Liu, X. Tian, J. De, T. Lu, Z. Yang, D. Zou, Y. Lv, S.-T. Zhang, Q. Su and B. Yang, *J. Mater. Chem. C*, 2021, **9**, 17511–17517.
74 V. Karunakaran and S. Das, *J. Phys. Chem. B*, 2016, **120**, 7016–7023.
75 Y. Gao, Y. Wang, Z. Guo, Y. Wan, C. Li, B. Yang, W. Yang and X. Ma, *J. Phys. Chem. B*, 2022, **126**, 2729–2739.
76 C.-W. Ju, B. Li, L. Li, W. Yan, C. Cui, X. Ma and D. Zhao, *J. Am. Chem. Soc.*, 2021, **143**, 5903–5916.
77 H. Gao, S. Shen, Y. Qin, G. Liu, T. Gao, X. Dong, Z. Pang, X. Xie, P. Wang and Y. Wang, *J. Phys. Chem. Lett.*, 2022, 7561–7567.
78 J. Bahrenburg, F. Renth, F. Temps, F. Plamper and W. Richtering, *Phys. Chem. Chem. Phys.*, 2014, **16**, 11549.
79 H.-M. Pan, C.-C. Wu, C.-Y. Lin, C.-S. Hsu, Y.-C. Tsai, P. Chowdhury, C.-H. Wang, K.-H. Chang, C.-H. Yang, M.-H. Liu, Y.-C. Chen, S.-P. Su, Y.-J. Lee, H. K. Chiang, Y.-H. Chan and P.-T. Chou, *J. Am. Chem. Soc.*, 2023, **145**, 516–526.

80 Y.-C. Wei, B.-H. Chen, R.-S. Ye, H.-W. Huang, J.-X. Su, C.-Y. Lin, J. Hodgkiss, L.-Y. Hsu, Y. Chi, K. Chen, C.-H. Lu, S.-D. Yang and P.-T. Chou, *Angew. Chem., Int. Ed.*, 2023, **62**, e202300815.

81 C. Fanggao, G. A. Saunders, E. F. Lambson, R. N. Hampton, G. Carini, G. Di Marco and M. Lanza, *J. Polym. Sci., Part B: Polym. Phys.*, 1996, **34**, 425–433.

82 M. Hénot, A. Chennevière, E. Drockenmuller, K. Shull, L. Léger and F. Restagno, *Eur. Phys. J. E*, 2017, **40**, 11.